# Super-Resolution Electrochemical Impedance Imaging with a $512 \times 256$ CMOS Sensor Array

Kangping Hu, Jason Ho, and Jacob K. Rosenstein School of Engineering Brown University, Providence, RI 02912, USA

Abstract—Super-resolution imaging is a family of techniques in which multiple lower-resolution images can be merged to produce a single image at higher resolution. While superresolution is often applied to optical systems, it can also be used with other imaging modalities. Here we demonstrate a  $512 \times 256$  CMOS sensor array for micro-scale super-resolution electrochemical impedance spectroscopy (SR-EIS) imaging. The system is implemented in standard 180 nm CMOS technology with a  $10 \,\mu\text{m} \times 10 \,\mu\text{m}$  pixel size. The sensor array is designed to measure the mutual capacitance between programmable sets of pixel pairs. Multiple spatially-resolved impedance images can then be computationally combined to generate a superresolution impedance image. We use finite-element electrostatic simulations to support the proposed measurement approach and discuss straightforward algorithms for super-resolution image reconstruction. We present experimental measurements of subcellular permittivity distribution within single green algae cells, showing the sensor's capability to produce microscale impedance images with sub-pixel resolution.

Keywords— Biosensor, impedance spectroscopy, superresolution, electrochemical, image sensor, CMOS, dielectric spectroscopy, impedance tomography, computational imaging

## I. INTRODUCTION

Electrochemical impedance spectroscopy (EIS) is an established technique to study processes occurring at an electrode surface, with numerous applications in cell culture monitoring [1]–[5] and bio-molecular diagnostics [6], [7], in addition to its established applications in electrochemistry. In many traditional EIS instruments, a potentiostat [8] is implemented with discrete electronics, and it is used to record the impedance at a working electrode (WE), corresponding to a single point in space. Compared to single-electrode EIS, spatially-resolved EIS can yield images with much richer information about a biological sample. Prior demonstrations of spatially-resolved EIS include examples using scanning probes [9] or small arrays of macro-scale electrodes [10] for impedance tomography.

More recently, high-density CMOS integrated electrode arrays [2], [11], [13] have become a popular EIS platform that can simultaneously offer high throughput, large field-of-view, fast acquisition rate, multimodal sensing capabilities, and low cost. However, since impedance imaging does not have the benefit of magnifying lenses, the ultimate imaging resolution of a CMOS sensor array is often determined by its

This work was supported in part by a grant from the Defense Advanced Research Projects Agency (DARPA), and by the National Science Foundation under Grant No. 2027108.

pixel spacing. In a given CMOS process node, the minimum dimensions of surface electrodes are generally larger than minimum transistor sizes. Adopting advanced process nodes and incorporating custom post-CMOS fabrication steps can improve the pixel resolution [11], [14], though this will inevitably increase the cost. Regardless of the sensor dimensions, it would be valuable to have techniques that can improve spatial resolution beyond the physical electrode spacing.

To address this challenge, we introduce a  $512 \times 256$  super-resolution electrochemical impedance spectroscopy (SR-EIS) CMOS sensor array which leverages concepts from widely-used approaches to construct a high-resolution image from multiple lower-resolution video frames [15]. A simplified conceptual diagram is shown in Fig. 1. Traditional EIS measures one working electrode at a time, but the proposed method measures the mutual capacitance between pairs of nearby

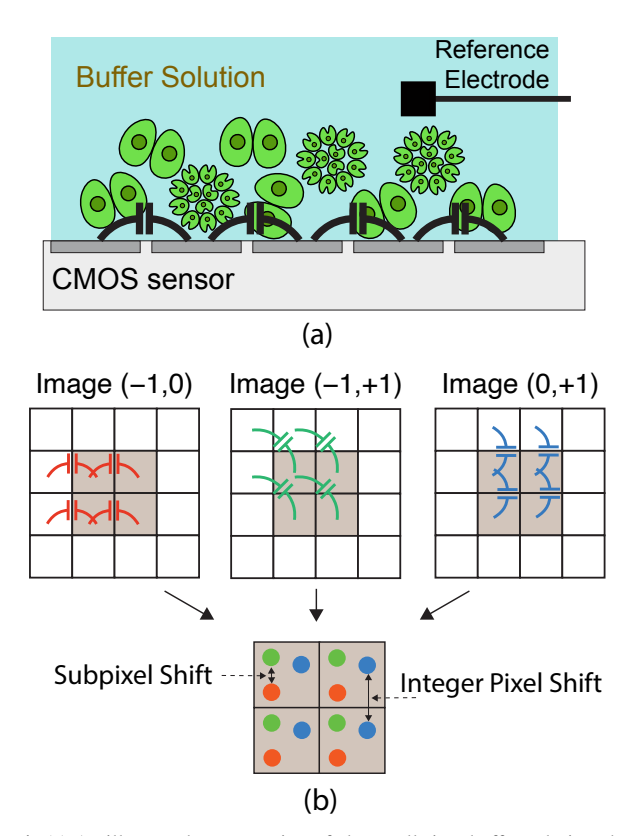


**Fig. 1:** (a) An illustrated cross-section of algae cells in a buffer solution above the sensor. The sensor is designed to measure the mutual capacitance between pairs of electrodes, and it produces spatially-resolved information about the dielectric permittivity and conductance of the sample. (b) Conceptual diagram of multiple mutual EIS image frames which are then assembled into one super-resolution EIS (SR-EIS) image.

pixels, allowing it to produce multiple frames which have subtle differences due to selecting different pixel pairs. For example, we can record an image that measures the mutual capacitance between each pixel and the pixel that is one position to its right; we can then generate another image that measures the mutual capacitance between each pixel and the pixel that is two positions to its right. The sensor array can be configured to measure between any arbitrary pair of pixels where the ultimate limit is set by the sensing depth. Each impedance image with different pairwise offsets possesses different information of the same scene as demonstrated in a finite-element-method (FEM) numerical simulation. Then we can use these multiple frames to computationally assemble a high-resolution composite image. This new scheme uses an area-efficient two-phase sensing scheme that fits into a 10  $\mu$ m pixel grid pitch. Compared to previous CMOS capacitance imaging arrays [2], [11], the new operating mode only requires two more switches per pixel. Similar to previous work, it can be configured to operate at radio frequency to overcome Debye screening and sense objects farther from the electrode surface. Mutual capacitance measurements have been previously used in Electrical Capacitance Tomography (ECT) with applications in flow imaging such as gas-solid flows [16] and trickle bed reactors [17]. However, earlier ECT systems have tended to have only a few macroscale electrodes and limited spatial resolution.

This is an extension of earlier work [18], which introduced SR-EIS using a  $100 \times 100$  CMOS sensor array. Here we have expanded the array size to  $512 \times 256$ , added new theoretical details and new experimental results, and introduced a new reconstruction algorithm. This paper is organized as follows. Section II explains the two-phase model and its measurement principle. Section III describes the detailed system architecture and the circuit design of a prototype SR-EIS implementation. Section IV shows the packaging and hardware setup of the measurement system. Section V compares FEM simulations with the EIS measurements on polystyrene microbeads. Section VI discusses the super-resolution reconstruction algorithm. Experimental measurements of single micro-algae are presented in Section VI, and Section VII concludes the paper.

#### II. TWO-PHASE MUTUAL CAPACITANCE SENSING

To illustrate the two-phase sensing scheme, we start with the single-pixel sensing model shown in Fig. 2(a) which presents one electrode capacitively coupled to a buffer solution.  $C_1$  is the capacitance seen by pixel #1, and two non-overlapping clocks  $\theta_1$  and  $\theta_2$  (Fig. 2(c)) rapidly charge and discharge  $C_1$  such that we can measure the sensing current with an integrating transimpedance amplifier (Fig. 2(d)). The value of  $C_1$  is expressed as:

$$C_1 = \frac{(V_{CM} - V_{BIAS})f_{sw}}{I_{SENSE}} \tag{1}$$

where  $f_{sw}$  denotes the switching frequency. This method only requires a few minimum-sized switches inside each pixel, and can scale easily with a small pixel pitch. In addition,

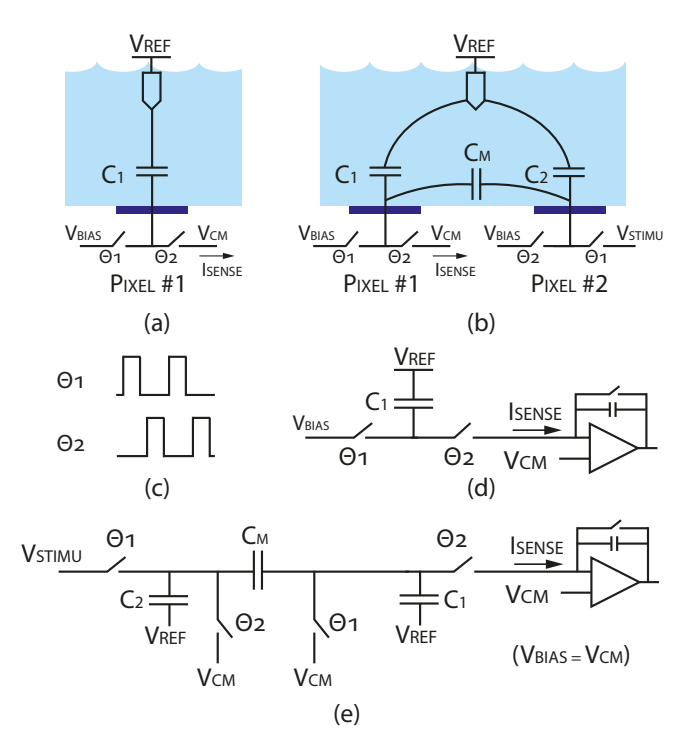


Fig. 2: Illustration of the single-pixel capacitance sensing versus the two-phase mutual capacitance sensing. (a) Single electrode with a simplified capacitance model. (b) Two adjacent electrodes with a simplified capacitance model. (c) The pixel switches are driven by two sets of non-overlapping clocks  $\theta_1$  and  $\theta_2$ . (d) Switched capacitor circuit to measure  $C_1$ . (e) If  $V_{BIAS} = V_{CM}$  and we swap the order of  $\theta_1$  and  $\theta_2$  in pixel #2, the circuit becomes equivalent to a parasitic-insensitive switched capacitor integrator, which measures  $C_M$ .

this circuit can operate at radio frequencies [2], [11], [12] to overcome Debye screening for farther detection depth. However, it only measures the capacitance between the pixel and the reference electrode. The mutual capacitance between adjacent pixels can be considered as a parasitic capacitance, which either adds to  $C_1$  or is intentionally shielded out, depending on how neighboring pixels are configured.

Since pixels can be capacitively coupled through fringe fields passing through the liquid media, the mutual capacitance may also contain rich information about the measured sample. We thus propose the two-phase mutual capacitance sensing shown in Fig. 2(b).  $C_1$  describes the capacitance that is only seen by electrode #1, and  $C_2$  is the capacitance that is only seen by electrode #2.  $C_M$  is the mutual capacitance between these two electrodes, which may include distributed electric fields extending into the sample as well as parasitic capacitance within the sensor chip. Since the electrodes are polarizable and the switching frequency ( $\geq 6.25 \, \mathrm{MHz}$ ) is faster than the typical  $10^{-6}$  sec relaxation time of electrical double layers in water [19], we assume that the response is primarily capacitive and we neglect distributed resistances in our analysis.

To support this sensing mode, there are a few modifications compared to single-pixel sensing. First, we exchange the roles of  $\theta_1$  and  $\theta_2$  that control the switches in pixel #2. Second, the second bias voltage of pixel #2 is connected to a global  $V_{STIMU}$  voltage reference. Finally, we set  $V_{BIAS} = V_{CM}$ . Interestingly, this circuit is equivalent to a classical non-inverting switched capacitor integrator as shown in Fig. 2(e).  $C_1$  and  $C_2$ 

do not contribute to the net output current  $(I_{SENSE})$ , and the mutual capacitance  $C_M$  can be expressed as:

$$C_M = \frac{(V_{CM} - V_{STIMU})f_{sw}}{I_{SENSE}} \tag{2}$$

which has an almost identical format as equation (1). This method inherits all the advantages from the single-pixel scheme, and the sensor can easily revert back to single-pixel sensing if pixel #2 is disabled and  $V_{BIAS}$  is set to a different voltage than  $V_{CM}$ . In the mutual capacitance mode, a reference electrode is not strictly required to bias the solution. By enabling the clocks and bias voltages appropriately, the mutual capacitance can be measured between any two pixels, whether or not they are immediately adjacent in the array.

Fig. 3 illustrates the process of scanning the sensor array to form one impedance image. In this simplified example, we use a  $3\times3$  kernel, where the grid indices of Pixel #1 and Pixel #2 from Fig. 2(b) are related by  $(i_2,j_2)=(i_1+\delta_i,j_1+\delta_j)$ , with  $\delta_i=\delta_j=1$ . This kernel is scanned over the entire array to generate an image. To produce a collection of images with slightly different dependence on the sample's spatially varying impedance, as described in Fig. 1, we can repeat the same process for different offset vectors  $(\delta_i,\delta_j)$ , and then vary the scanned pattern to create multiple different impedance perspectives.

The kernel size is ultimately limited by the fact that the mutual capacitance decreases with the distance between pixel pairs. To acquire all pairwise  $N \times N$  kernels requires measuring  $N^2$ -1 images, and the control logic to scan the appropriate address through the array can be implemented easily with a few shift registers, supporting a fast frame rate as shown in the next section.

Although here we focus on the mutual capacitance between exactly two pixels, the two-phase capacitance sensing can also be applied to more than two pixels at a time, creating more complex fringe fields [20]. Multi-pixel switching patterns could enable enhanced sensing modes or in-pixel computations, or perhaps find more efficient image sets with fewer than N<sup>2</sup>-1 frames.

## III. CMOS SENSOR ARRAY DESIGN

#### A. Pixel and Array

Simplified schematics of the sensor array are shown in Fig. 4. The active sensing area has 131,072 pixels arranged in a  $256 \times 512$  array. Note that in our earlier SR-EIS demonstration

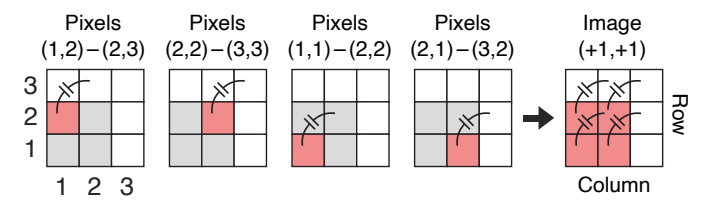


**Fig. 3:** One EIS image is constructed from a collection of pairwise mutual capacitance measurements. Illustrated above is the construction of the image which measures  $C_M$  between each pixel and one of its diagonal neighbors, which we describe as a kernel offset of  $(\delta_i, \delta_j)$ =(+1,+1). Different kernels can be used to produce different EIS images, as illustrated in Fig. 1b.

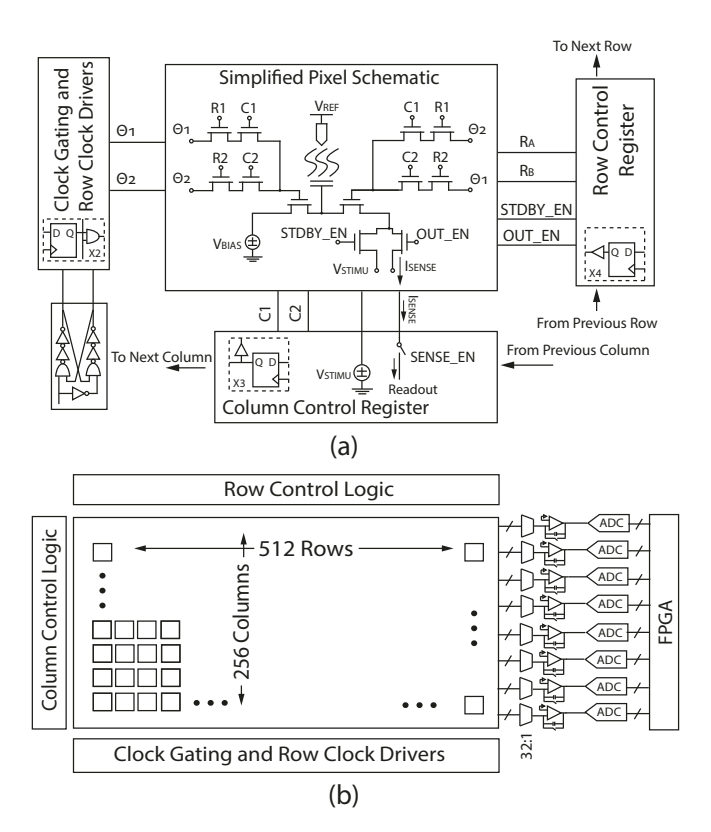


Fig. 4: (a) Simplified SR-EIS pixel and array schematic. The pixels are controlled by row-wise and column-wise control signals, with shift register logic to support scanning through the array. (b) Architecture of the  $256 \times 512$  pixel sensor array, including the column readout signal paths.

[18], we used a smaller  $100 \times 100$  array. This new larger sensor has multiple sensing and stimulation modes, but here we only focus on SR-EIS using the chip's mutual-capacitance measurement mode. More details on the other features of the sensor can be found in [21].

Each pixel shown in Fig. 4(a) can be driven by a pair of on-chip non-overlapping clocks  $\theta_1$  and  $\theta_2$ , with the option to swap the positions of the two clocks, as described earlier. A reference clock is provided from an external FPGA, and the array includes an on-chip two-phase clock generator with 4bit trimming of the non-overlap time. A set of shift registers are used to control the row clock gating and row-wise control signals, thereby controlling the clock polarity and the output routing of each pixel. Different pairwise measurement offset kernels can be configured by initializing the corresponding shift registers. To acquire each impedance image, we scan the entire array in a column-first, row-last addressing order starting from the initial shift register values. All switches are implemented with minimum-sized NMOS transistors for area efficiency.  $\theta_1$  and  $\theta_2$  are held low for a brief period of time before each pixel measurement to fully discharge the NMOS switch gates to prevent any stored charge in the pass-gate controlled clock paths from interfering with the next pixel scan.

# B. Readout Circuit

The readout circuit shown in Fig. 4(b) is composed of eight parallel channels to improve the frame rate, with each channel multiplexed between 32 columns. Each readout path

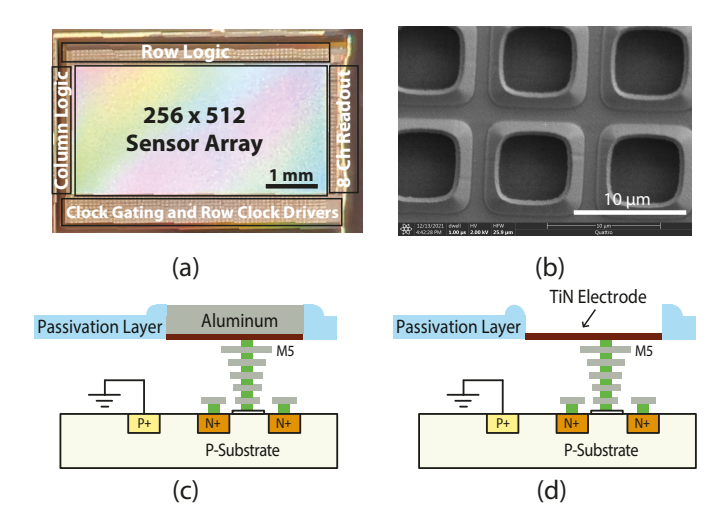


**Fig. 5:** (a) Die photo of the  $256 \times 512$  pixel sensor array. (b) SEM image of electrodes. (c) Cross-section of an electrode before aluminum etching. (d) Cross-section of an electrode after etching the aluminum, and exposing a TiN layer as the sensing surface.

includes a pair of integrators followed by buffers to drive eight external 500 kS/s 18-bit ADCs. Correlated double sampling and chopping are applied to suppress offsets and 1/f noise.

#### IV. HARDWARE IMPLEMENTATION

#### A. Layout and Packaging

The circuit is implemented in a 180 nm 1P6M CMOS process, occupying  $25 \ mm^2$ , including  $13.1 \ mm^2$  active sensing area. (Fig. 5(a)). We adopted a one-step post-processing procedure as previously described [2], [22]. After encapsulating the wirebonds in epoxy, a simple open-top fluidic cell is assembled around the sensor and the aluminum top metal is chemically removed to expose a titanium nitride (TiN) electrode surface (Fig. 6(c)), because aluminum can be easily corroded while TiN is chemically stable. The cross-section view of the electrode is shown in Fig. 5(c)(d). A scanning electrode microscope image of several electrodes after post-processing is shown in Fig. 5(b).

#### B. Hardware Setup

The sensor array chip is wire-bonded to a small printed circuit board module, which is connected to a larger PCB hosting an FPGA module (Opal Kelly XEM7310), eight analog-to-digital converters (ADS8881), a multi-channel DAC for setting bias voltages (LTC2636), and power regulation. The entire system is powered by a single 5V power supply and it is controlled over USB 3.0 by a computer within a Python environment. (Fig. 6(b)). The sensor chip consumes 58.8 mW, and the data acquisition board plus FPGA module together draw 1.2 W.

# V. EXPERIMENTS AND SIMULATIONS WITH MICROSPHERES

To better understand the mutual capacitance imaging modes, we performed experiments with polystyrene microspheres, as well as corresponding electrostatic simulation using the pyEIT framework [23]. The experimental and simulated results showed good correspondence, as shown in Fig. 7.

In the measurement, 20  $\mu$ m polystyrene beads are dispersed in 1× phosphate buffered saline (PBS) and allowed to settle onto the sensor array. Using the inspection microscope, we identified two beads, one of which was directly over a pixel while the other landed halfway between two pixels (Fig. 7(a)). The switching frequency was set to 6.25 MHz which is high enough to overcome Debye shielding while staying within the bandwidth of the readout circuits. We aimed to maximize the signal while not saturating the readout signal paths, and selected  $\Delta V = 300$  mV. We measured slices of mutual capacitance images within a linear array of 11 pixels beneath the beads, using offsets ranging from 1 through 5 ( $\delta_i = 0$ ,  $1 \leq \delta_i \leq 5$ ). The measured results for each offset kernel are shown in Fig. 7(c). We also performed electrostatic simulations using pyEIT, using a similar electrode geometry and the same two types of bead locations. The background permittivity was set to  $\epsilon_r = 80$ , the bead permittivity was set to  $\epsilon_r = 2.5$ , and the simulation used a triangular mesh with 2986 nodes and 5748 elements (Fig. 7(b)(d)). The simulations focus on bulk properties, and do not include surface charges or double layers on the beads or electrodes. We believe these simplifications are acceptable for these geometries at the MHz switching frequencies of the sensor.

We can see that the measurement agrees reasonably well with the simulation. In both the measurements and simulation, the mutual capacitance shows significant differences between the two scenarios, despite the sub-pixel movement of the bead. The changes in mutual capacitance also appear to be qualitatively different for each pixel spacing, suggesting that distinct information is contained in each measurement configuration. Some of the difference is due to the fact that the electrode spacing is under-sampling the permittivity space,

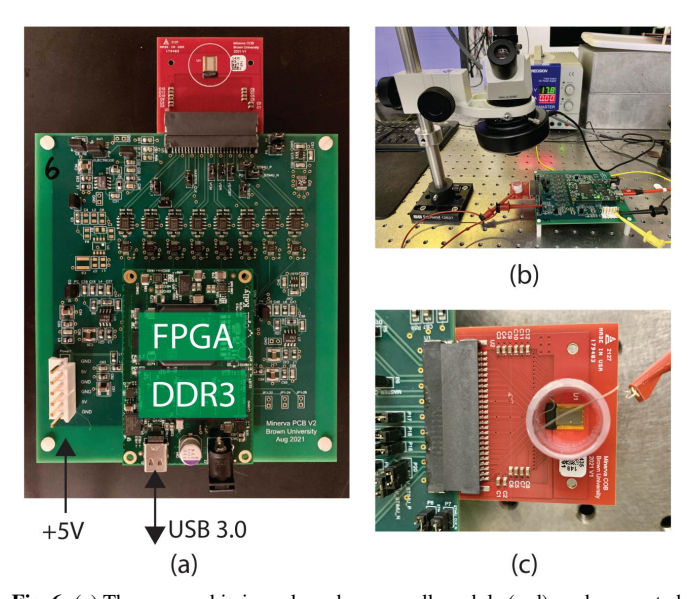


**Fig. 6:** (a) The sensor chip is packaged on a small module (red), and connected to a larger data acquisition board (green). (b) Experiments are performed under a simple inspection microscope, for simultaneous optical observation. (c) The sensor is assembled with a simple fluid chamber and a silver/silver-chloride pseudo reference electrode.

and we expect that if there were finer electrode spacing for the same  $20 \,\mu\text{m}$  microspheres, then the red curve (bead centered on a pixel) would be a shifted version of the black curve (bead between two pixels).

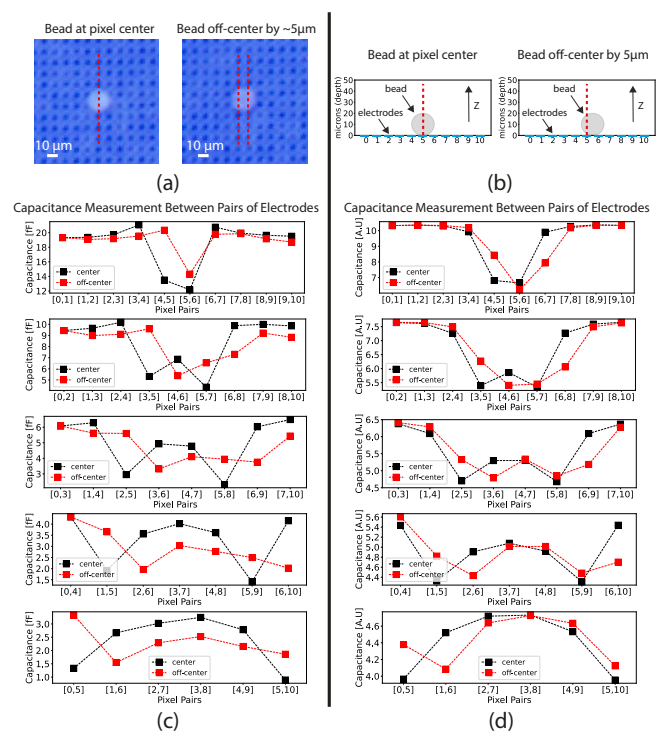


Fig. 7: (a) Two  $20 \,\mu m$  diameter polystyrene beads immersed in  $1 \times PBS$  buffer on the sensor array, with one bead placed right on top of an electrode, and the other positioned with  $5 \,\mu m$  offset halfway between two electrodes. (b) Simulation to mimic the scenarios in (a), using pyEIT [23]. (c) Mutual capacitance measurements between pairs of electrodes in a linear 11-element array, with pixel spacing ranging from 1-5 for the bead at the pixel center. (d) Simulated results with the bead halfway between pixels.

Another level of understanding can come from looking at the electric field distribution during these mutual capacitance measurements. In Fig. 8(a) we simulate the electric field during the [0,1] measurement from Fig. 7(c). The nonlinear decay of field intensity with distance means that the presence of the bead has relatively little influence on the measured capacitance. In contrast, Fig. 8(b) shows the measurement [5,6], in which the electric field is much stronger within the bead, and its lower local permittivity results in a lower measured capacitance than if there had been no bead. When there is larger spacing between pixel pairs, the lateral size of the observed decrease becomes wider because the electric field intensity extends farther into the sample. When the pixel pairs are even farther apart (e.g.  $\delta_i = 4$ ), the electric field is stronger near the two pixels but weaker at their midpoint, producing the observed bimodal capacitance profile.

# VI. SUPER-RESOLUTION IMPEDANCE IMAGING

# A. Imaging Unicellular Algae

Algae cells are interesting creatures with a diversity of shapes and sizes, which make them useful for impedance imaging [24]. Here we use a mix of *Cosmarium* and *Pediastrum* (Carolina Biological, NC, USA) to demonstrate

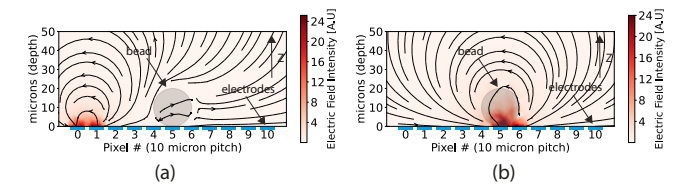


**Fig. 8:** Finite element simulation (using pyEIT [23]) to compare the bead's effect on the electric field distribution between pixels [0,1](a) and between pixels [5,6](b).

the effectiveness of the proposed super-resolution impedance imaging. Both of these green microalgae have intermediate cell size (approximately  $10 \, \mu \text{m} - 50 \, \mu \text{m}$  diameter). *Cosmarium* has a bi-lobal shape, while *Pediastrum* is mostly observed in small clusters of several dozen cells (Fig. 9).

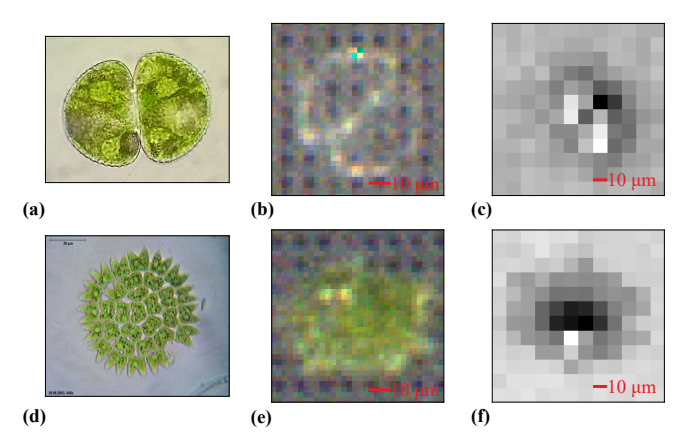
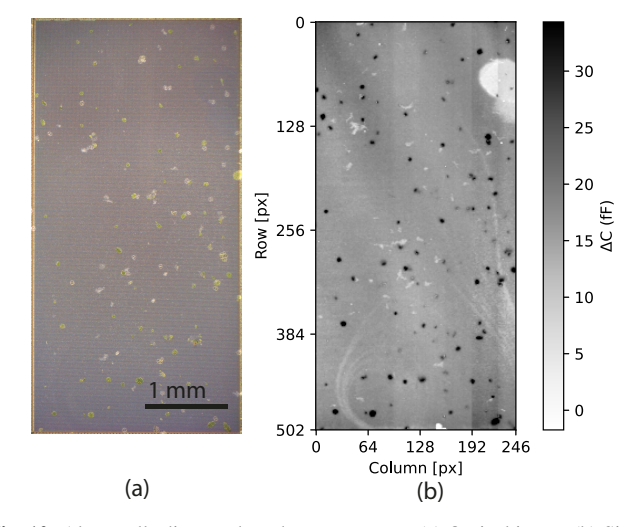


Fig. 9: Images of two types of green algae. (a) A reference image of Cosmarium. (Atriplex82, CC BY-SA 4.0, via Wikimedia Commons.) (b) An optical microscope image of one cosmarium cell on the sensor array. (c) A single impedance image of the cosmarium cell from b. (d) A reference optical image of a cluster of pediastrum cells. (Dr. Ralf Wagner, CC BY-SA 3.0, via Wikimedia Commons) (e) An optical image of a cluster of pediastrum cells on the sensor array. (f) A single impedance image of the pediastrum cluster.



**Fig. 10:** Algae cells dispersed on the sensor array. (a) Optical image (b) Single frame EIS image with (+1,+1) offset. Ten rows and columns at the edge are cropped due to the  $11 \times 11$  kernel size.

An optical image of the mixed algae sample dispersed on the sensor is shown in Fig. 10(a), alongside a single frame EIS image of the same sample (Fig. 10(b)). For the EIS imaging,  $V_{CM} = V_{BIAS} = 500$  mV,  $V_{STIMU} = 300$  mV, and

the switching frequency is 3.125 MHz. It is relatively simple to differentiate these two types of algae from their colors in the optical image, but at first glance, they appear to be very similar in the EIS image.

In Fig. 11 and Fig. 12, we zoom in on one *Cosmarium* cell and one *Pediastrum* cell. These experiments were optimized for resolution rather than frame rate, and we set the integration time to  $50\,\mu s$ , which meant we could acquire one  $512\times256$  image every 7 seconds. Each offset leads to a different perspective of the same target cell, providing signal diversity and sub-pixel information which we can exploit for superresolution reconstruction.

In practice, the fact that the mutual capacitance decreases super-linearly with distance [18] creates diminishing returns to using very large kernel sizes. For example, in Fig.7(c) we can observe that the mutual capacitance at  $50\,\mu\mathrm{m}$  pixel separation is ten times smaller than at  $10\,\mu\mathrm{m}$  separation. As a compromise between signal strength and the total acquisition time, we selected an  $11\times11$  kernel size. With this kernel size, measuring a full stack of 120 mutual capacitance images took a total of 17 minutes.

# B. Reconstruction Algorithm

Many techniques have been developed for assembling a high-resolution optical image from lower-resolution images of the same scene. For example, multiple video frames can be aligned and computationally merged, taking advantage of the fact that camera motion produces spatial shifts in the scene relative to the image sensor which can yield a higher resolution composite image than the individual frames [15]. The primary technical challenge lies in predicting the subpixel motion to realign images. In our application, the collection of EIS images additionally appears to include other subtle distortions beyond a simple shift.

We produced a composite super-resolution impedance image using a procedure that involves (1) upsampling the original

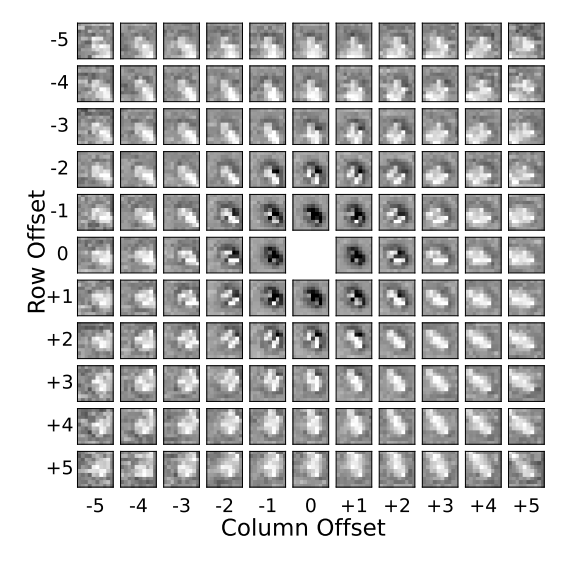


**Fig. 11:** Cosmarium impedance images. A collection of 120 impedance images of one Cosmarium cell were acquired with offset kernels  $(\delta_i, \delta_j)$  varied between  $-5 < \delta_i < +5$  and  $-5 < \delta_j < +5$ . While these are all images of the same cell, each offset kernel produces a different perspective. Note the spatial distortion of the algae based on the offset kernel.

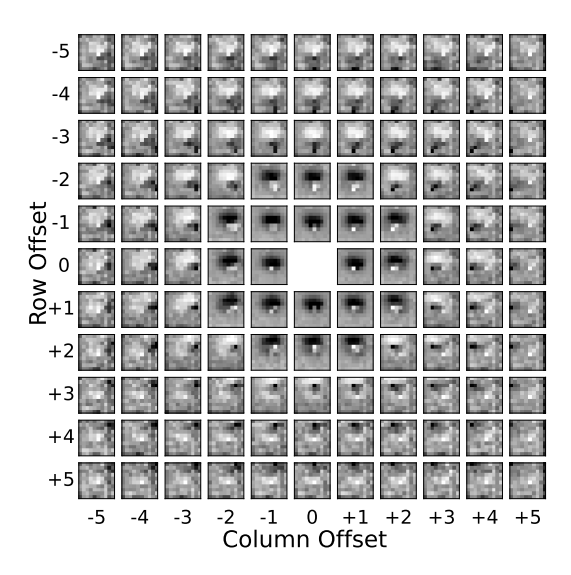


**Fig. 12:** Pediastrum impedance images. A collection of 120 impedance images of one Pediastrum cell cluster were acquired with offset kernels  $(\delta_i, \delta_j)$  varied between  $-5 < \delta_i < +5$  and  $-5 < \delta_j < +5$ . While these are all images of the same cluster, each offset kernel produces a different perspective. Note the spatial distortion of the algae based on the offset kernel.

EIS images, (2) computing a linear filter to align each image to a common reference EIS image, (3) summing the re-aligned EIS images, and (4) applying a high-pass filter to compensate for interpolation on the original low-resolution EIS images.

Simply summing the multiple raw EIS images would result in smearing due to the spatial distortion produced from the different offset kernel mutual impedance images. To address this distortion and improve the alignment, we performed a linear deconvolution to approximate a filter that would undo the distortion of each image. We note that convolution operations performed in the spatial domain are equivalent to multiplication in the spatial frequency domain. Therefore, if we let a(x,y) and r(x,y) represent our input and output signals, respectively, and A(u,v) and R(u,v) represent their frequency domain representations, the linear filter, H, can be expressed as:

$$H(u,v) = \frac{R(u,v)}{A(u,v)} \tag{3}$$

The common reference image is selected as one with a small offset vector (e.g. (+1,+1), and it approximates the expected output signal with minimal spatial distortion. If  $a_i(x,y)$  represents our input upsampled high-passed image, r(x,y) represents our upsampled high-passed signal reference, and w(x,y) represents a zero-padded Hanning window to reduce spectral leakage, our algorithm for N images can be expressed as:

$$b(x,y) = \sum_{i=1}^{N} a_i(x,y) * \left( F^{-1} \left[ \frac{F(r(x,y))}{F(a_i(x,y))} \right] \cdot w(x,y) \right)$$
 (4)

where b(x,y) is the computed SR-EIS image. The spatial alignment filter simultaneously solves for both lateral shifts and some types of image distortion between different offset kernels.

In Fig. 13 and Fig. 14, we apply this super-resolution algorithm to three instances of each of the two algae species,

with N=120. Although not all of the single raw images of Cosmarium reveal their two hemispheres, these were three of the examples where the bi-lobal structure was the most apparent in the raw images. Their respective SR-EIS images further enhance the bi-lobal structure while rounding the overall shape of the cell, consistent with microscopy images. For Pediastrum, single raw EIS images were unable to resolve individual cells within clusters. In the computed SR-EIS images, we were able to resolve more detail in the shape of the cluster, with irregular boundary shapes which likely correspond to 'missing' single cells from the edges of the cluster (similar to Fig. 9(d)). We notice that cells may appear darker (lower impedance) for short offset vectors, but lighter (higher impedance) for larger offset vectors. This observation may relate to the cells' 3-D shapes, as longer offset vectors have fringe fields that penetrate deeper into the sample [18]. This difference in polarity also leads to the dark outlines of the algae in the SR-EIS Pediastrum images. The composite images contain significantly more spatial information than the single *Pediastrum* images, although a precise physical interpretation of the spatial impedance profiles is complicated by the intensity and polarity changes with different offsets.

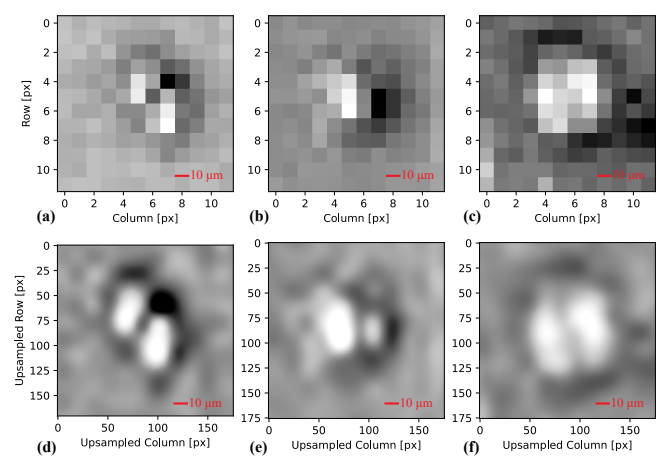


**Fig. 13:** Super-resolution impedance (SR-EIS) reconstruction of three *Cosmarium* cells with their respective raw impedance reference. (a) Impedance image with offset kernel  $(\delta_i, \delta_j) = (-2, 0)$  (b) Impedance image with offset kernel  $(\delta_i, \delta_j) = (-2, -1)$  (c) Impedance image with offset kernel  $(\delta_i, \delta_j) = (-3, -1)$  (d, e, f) Linear deconvolution algorithm applied on 120 impedance images with reference image defined in (a,b,c).

Investigating the SR-EIS image features further, we took linear slices through the composite and reference EIS images for *Cosmarium* and *Pediastrum* (Fig. 15). The *Cosmarium* composite image slice shows improved resolution with a similar profile as the single-frame EIS image and confirms that the one-pixel features in the lower-resolution image are in fact the two hemispheres of the *Cosmarium*. For *Pediastrum*, the line profile once again highlights that the composite image includes finer spatial features within one cluster of cells. However, as mentioned previously, providing a physical explanation for the lower-impedance outline around the cell cluster remains an open challenge.

While these preliminary results are promising, we anticipate that further improvements could be achieved with improved reconstruction algorithms. For example, there ought to be

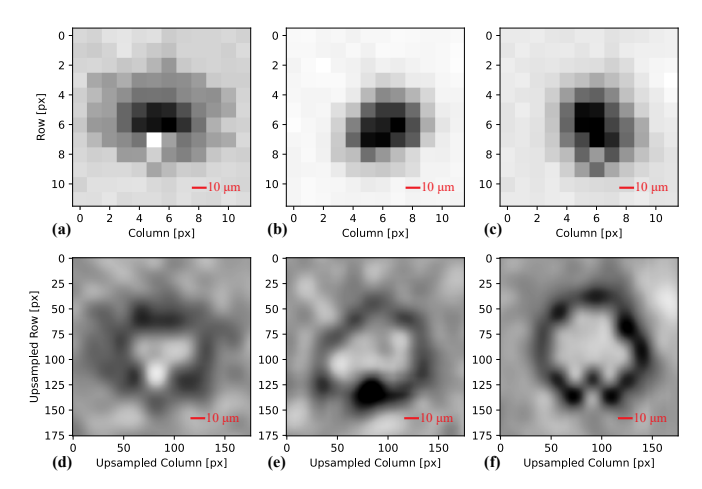
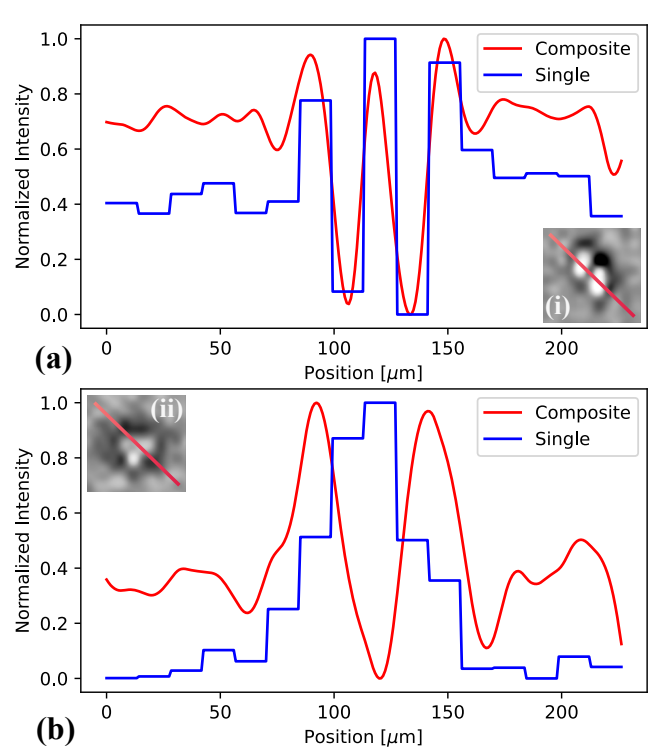


Fig. 14: Super-resolution reconstruction of three pediastrum cells with their respective raw impedance reference. Offset kernel is chosen to show algae well in raw images. (a) Impedance image with offset kernel  $(\delta_i, \delta_j) = (+1, +1)$ . (b) Impedance image with offset kernel  $(\delta_i, \delta_j) = (+1, 0)$ . (c) Impedance image with offset kernel  $(\delta_i, \delta_j) = (+1, 0)$ . (d, e, f) Linear deconvolution algorithm applied on 120 impedance images with reference image defined in (a.b.c).



**Fig. 15:** Algae line profile of a single EIS frame vs. composite SR-EIS. (a) Cosmarium slice taken across the isthmus to highlight its bi-lobal structure. The single EIS frame used has kernel offset  $(\delta_i, \delta_j) = (-2, 0)$ . (b) Pediastrum through same slice with single EIS frame with kernel offset  $(\delta_i, \delta_j) = (+1, +1)$ .

radial symmetries and scaling trends across the multiple EIS images which are not currently enforced in the deconvolution filter solutions. It may also be worthwhile to pursue alternative super-resolution reconstruction techniques that could allow for nonlinear alignment filters, such as those built on deep learning models [30].

TABLE I: Survey of Super-Resolution Imaging Sensor Arrays

	[25]	[26]	[27]	[28]	[29]	this work
Application	Microfluidic	Contact	Time-of-Flight	Near-Field	Satellite	Electrochemical
	Cytometer	Scanning	3-D Camera	Imaging	Remote Sensing	Imaging
Operating	Single-Frame	Staggered Pixel	Background Light	Confined E-field	Interlaced Pixel	Mutual
Principle	Machine-Learning	Multi-line Scanner	Suppression	of Oscillator		Capacitance
Measurement Mode	Optical	Optical	Optical	Terahertz	Optical	EIS
Sample Type	Blood Cell	Bubbles	3-D Object	Nickel Mesh	3-D Object	Algae Cells
Sensor Process	65 nm BSI	$0.35\mu\mathrm{m}$ CMOS	$0.11\mu\mathrm{m}$ CIS	0.13 μm SiGe	$0.18\mu\mathrm{m}$ CIS	$0.18\mu\mathrm{m}$ CMOS
Pxel Size	$1.1 \times 1.1 \mu{\rm m}$	$8\times11\mu\mathrm{m}$	$5.9 \times 5.9 \mu\mathrm{m}$	$25\times25\mu\mathrm{m}$	6×6 μm	$10\times10\mu\mathrm{m}$
Array Size	1600×2056	256×214	336×256	2×64	128×8×2	512×256
Fill Factor	0.15	0.21	0.24	0.48	0.27	0.52
Power	182.8 mW	60 μW per column	680 mW	37–104 mW	4.114 μW per column	58.8 mW

#### VII. CONCLUSION

In this paper, we have presented a new approach for spatially-resolved electrochemical impedance imaging with a 512 × 256 CMOS EIS sensor array. A survey of several other types of super-resolution sensors is listed in Table-I. To support the SR-EIS imaging mode, we introduced an area-efficient pixel design supporting arbitrary programmable mutual capacitance measurements. We used FEM simulation and experiments with polystyrene microspheres to validate the sensor's ability to extract sub-pixel information. As a demonstration, we presented state-of-the-art non-optical measurements of unicellular algae Cosmarium and Pediastrum, producing super-resolution impedance images with linear reconstruction algorithms that resolve spatial features smaller than the sensor array's pixel pitch, including some sub-cellular structures. Future work will include exploring more advanced algorithms for super-resolution image reconstruction, and 3D shape reconstruction. A wide range of biomedical applications may stand to benefit from spatially resolved super-resolution EIS imaging.

#### VIII. ACKNOWLEDGEMENT

The authors thank Pushkaraj Joshi for electron microscopy, and Christopher Arcadia, Joseph Larkin, and Sherief Reda for technical discussions.

#### REFERENCES

- [1] O. A. K'Owino, I. O.; Sadik, "Impedance spectroscopy: a powerful tool for rapid biomolecular screening and cell culture monitoring," *Electroanalysis*, vol. 17, pp. 2101–2113, 2005.
- [2] K. Hu, C. E. Arcadia, and J. K. Rosenstein, "A large-scale multimodal-CMOS biosensor array with 131,072 pixels and code-division multi-plexed readout," *IEEE Solid-State Circuits Letters*, vol. 4, pp. 48–51, 2021.
- [3] J. S. Park, M. K. Aziz, S. Li, T. Chi, S. I. Grijalva, J. H. Sung, H. C. Cho, and H. Wang, "1024-pixel CMOS multimodality joint cellular sensor/stimulator array for real-time holistic cellular characterization and cell-based drug screening," *IEEE Transactions on Biomedical Circuits and Systems*, vol. 12, no. 1, pp. 80–94, 2018.
- [4] B. P. Senevirathna, S. Lu, M. P. Dandin, J. Basile, E. Smela, and P. A. Abshire, "Real-time measurements of cell proliferation using a lab-on-cmos capacitance sensor array," *IEEE Transactions on Biomedical Circuits and Systems*, vol. 12, no. 3, pp. 510–520, 2018.
- [5] C. Laborde, F. Pittino, H. A. Verhoeven, S. G. Lemay, L. Selmi, M. A. Jongsma, and F. P. Widdershoven, "Real-time imaging of microparticles and living cells with CMOS nanocapacitor arrays," *Nature Nanotechnology*, vol. 10, p. 791, aug 2015.
- [6] S. B. Prakash and P. Abshire, "Tracking cancer cell proliferation on a CMOS capacitance sensor chip," *Biosensors and Bioelectronics*, vol. 23, no. 10, pp. 1449–1457, 2008.
- [7] A. Romani, N. Manaresi, L. Marzocchi, G. Medoro, A. Leonardi, L. Altomare, M. Tartagni, and R. Guerrieri, "Capacitive Sensor Array for Localization of Bioparticles in CMOS Lab-on-a-Chip," ISSCC, 2004.

- [8] R. Turner, D. Harrison, and H. Baltes, "A CMOS potentiostat for amperometric chemical sensors," *IEEE Journal of Solid-State Circuits*, vol. 22, no. 3, pp. 473–478, 1987.
- [9] D. T. Anthony Layson, Shailesh Gadad, "Resistance measurements at the nanoscale: scanning probe ac impedance spectroscopy," *Electrochimica Acta*, vol. 48, pp. 2207–2213, 2003.
- [10] J. Ye, H. Wang, and W. Yang, "Image reconstruction for electrical capacitance tomography based on sparse representation," *IEEE Transactions* on *Instrumentation and Measurement*, vol. 64, no. 1, pp. 89–102, 2015.
- [11] F. Widdershoven, A. Cossettini, C. Laborde, A. Bandiziol, P. P. van Swinderen, S. G. Lemay, and L. Selmi, "A CMOS pixelated nanocapacitor biosensor platform for high-frequency impedance spectroscopy and imaging," *IEEE transactions on biomedical circuits and systems*, vol. 12, no. 6, pp. 1369–1382, 2018.
- [12] K. Hu, E. Kennedy, and J. K. Rosenstein, "High frequency dielectric spectroscopy array with code division multiplexing for biological imaging," in 2019 IEEE Biomedical Circuits and Systems Conference (BioCAS). IEEE, 2019, pp. 1–4.
- [13] J. Abbott, A. Mukherjee, W. Wu, T. Ye, H. S. Jung, K. M. Cheung, R. S. Gertner, M. Basan, D. Ham, and H. Park, "Multi-parametric functional imaging of cell cultures and tissues with a CMOS microelectrode array," *Lab on a Chip*, vol. 22, no. 7, pp. 1286–1296, 2022.
- [14] K. Niitsu, S. Ota, K. Gamo, H. Kondo, M. Hori, and K. Nakazato, "Development of microelectrode arrays using electroless plating for CMOS-based direct counting of bacterial and hela cells," *IEEE transactions on biomedical circuits and systems*, vol. 9, no. 5, pp. 607–619, 2015.
- [15] S. C. Park, M. K. Park, and M. G. Kang, "Super-resolution image reconstruction: a technical overview," *IEEE Signal Processing Magazine*, vol. 20, no. 3, pp. 21–36, 2003.
- [16] T. Dyakowski, R. Edwards, C. Xie, and R. A. Williams, "Application of capacitance tomography to gas-solid flows," *Chemical Engineering Science*, vol. 52, no. 13, pp. 2099–2110, 1997.
- [17] N. Reinecke and D. Mewes, "Investigation of the two-phase flow in trickle-bed reactors using capacitance tomography," *Chemical engineering science*, vol. 52, no. 13, pp. 2111–2127, 1997.
- [18] K. Hu, C. E. Arcadia, and J. K. Rosenstein, "Super-resolution electrochemical impedance imaging with a 100 × 100 CMOS sensor array," in 2021 IEEE Biomedical Circuits and Systems Conference (BioCAS), 2021, pp. 1–4.
- [19] J. O. Bockris, E. Gileadi, and K. Müller, "Dielectric relaxation in the electric double layer," *The Journal of Chemical Physics*, vol. 44, no. 4, pp. 1445–1456, 1966.
- [20] K. Hu, C. E. Arcadia, and J. K. Rosenstein, "A fringe field shaping cmos capacitive imaging array," in 2021 IEEE Sensors, 2021, pp. 1–4.
- [21] K. Hu, J. Incandela, X. Lian, J. W. Larkin, and J. K. Rosenstein, "A 13.1 mm 2 512× 256 multimodal cmos array for spatiochemical imaging of bacterial biofilms," in 2022 IEEE Custom Integrated Circuits Conference (CICC). IEEE, 2022, pp. 1–2.
- [22] K. Hu, X. Lian, S. Dai, and J. K. Rosenstein, "Low noise CMOS isfets using in-pixel chopping," in 2019 IEEE Biomedical Circuits and Systems Conference (BioCAS). IEEE, 2019, pp. 1–4.
- [23] B. Liu, B. Yang, C. Xu, J. Xia, M. Dai, Z. Ji, F. You, X. Dong, X. Shi, and F. Fu, "pyeit: A python based framework for electrical impedance tomography," *SoftwareX*, vol. 7, pp. 304–308, 2018.
- [24] C. E. Arcadia, K. Hu, S. Epstein, M. Wanunu, A. Adler, and J. K. Rosenstein, "CMOS electrochemical imaging arrays for the detection and classification of microorganisms," in 2021 IEEE International Symposium on Circuits and Systems (ISCAS), 2021, pp. 1–5.
- [25] X. Liu, X. Huang, Y. Jiang, H. Xu, J. Guo, H. W. Hou, M. Yan, and H. Yu, "A microfluidic cytometer for complete blood count with a 3.2megapixel, 1.1- m-pitch super-resolution image sensor in 65-nm bsi cmos,"

- *IEEE Transactions on Biomedical Circuits and Systems*, vol. 11, no. 4, pp. 794–803, 2017.
- [26] C. W. Liu, A. Feizi, N. Sarhangnejad, G. Gulak, and R. Genov, "Superresolution line scan image sensor for multimodal microscopy," *IEEE Transactions on Biomedical Circuits and Systems*, vol. 12, no. 5, pp. 1165–1176, 2018.
- [27] J. Cho, J. Choi, S.-J. Kim, S. Park, J. Shin, J. D. K. Kim, and E. Yoon, "A 3-d camera with adaptable background light suppression using pixelbinning and super-resolution," *IEEE Journal of Solid-State Circuits*, vol. 49, no. 10, pp. 2319–2332, 2014.
- [28] P. Hillger, R. Jain, J. Grzyb, W. Försterr, B. Heinemann, G. MacGrogan, P. Mounaix, T. Zimmer, and U. R. Pfeiffer, "A 128-pixel system-on-a-chip for real-time super-resolution terahertz near-field imaging," *IEEE Journal* of Solid-State Circuits, vol. 53, no. 12, pp. 3599–3612, 2018.
- [29] J.-H. Chang, K.-W. Cheng, C.-C. Hsieh, W.-H. Chang, H.-H. Tsai, and C.-F. Chiu, "Linear cmos image sensor with time-delay integration and interlaced super-resolution pixel," in SENSORS, 2012 IEEE, 2012, pp. 1–4.
- [30] Z. Wang, J. Chen, and S. C. Hoi, "Deep learning for image superresolution: A survey," *IEEE transactions on pattern analysis and machine* intelligence, vol. 43, no. 10, pp. 3365–3387, 2020.



**Kangping Hu** (S'18) received the B.S. degree (*summa cum laude*) in electrical engineering and computer engineering from Boston University, MA, USA, in 2013, the M.S. degree in electrical engineering from California Institute of Technology, CA, USA, in 2014, and the M.S. degree in computer science from Brown University, RI, USA. Currently, he is pursuing the Ph.D. degree at Brown University, RI USA

From 2015 to 2022, he has worked as an RFIC engineer at Calterah Semiconductor on 77GHz CMOS

Radar, a DRAM design engineer at Micron Technology on LPDDR4/5, a research intern at Meta Reality Lab, and a 3-time hardware intern at Apple. His current research interests include the design and modeling of mixed-

His current research interests include the design and modeling of mixedsignal integrated circuit and multi-modal sensor array platform for bio-sensing applications.



**Jason Ho** (S'21) is pursuing an Sc.B. in computer engineering at Brown University, RI, USA, set to graduate in 2022. Afterwards, he will work toward a Ph.D. in electrical and computer engineering.

In the past, he has worked as an FPGA engineering intern at Nabsys 2.0 and as a VLSI design intern at Seagate Technology on signal processing pipeline microarchitectures.

His current research interests include ultra low power computing, energy-efficient computing systems, and organic approaches to computing such as

neuromorphic computing systems.



Jacob K. Rosenstein Jacob K. Rosenstein is an Associate Professor of Engineering at Brown University in Providence, RI. He received Sc.M. and Ph.D. degrees in electrical engineering from Columbia University, and an Sc.B in Computer Engineering from Brown University. He previously worked as a hardware systems engineer at Analog Devices Inc. and MediaTek Wireless Inc. His current research interests include biomedical electronics, mixed-signal circuit design, and chemical information systems.